



Disc-halo gas outflows driven by stellar clusters as seen in multiwavelength tracers

Evgenii O. Vasiliev ¹,^{*} Sergey A. Drozdov,¹ Biman B. Nath ², Ralf-Jürgen Dettmar³
and Yuri A. Shchekinov^{1,2}

¹*Lebedev Physical Institute of Russian Academy of Sciences, 53 Leninsky Ave., 119991, Moscow, Russia*

²*Raman Research Institute, C. V. Raman ave., Sadashiva Nagar, Bangalore 560080, India*

³*Ruhr University Bochum, Faculty of Physics and Astronomy, Astronomical Institute (AIRUB), Universitätsstrasse 150, D-44780 Bochum, Germany*

Accepted 2023 January 25. Received 2023 January 18; in original form 2022 October 30

ABSTRACT

We consider the dynamics of and emission from growing superbubbles in a stratified interstellar gaseous disc driven by energy release from supernovae explosions in stellar clusters with masses $M_{cl} = 10^5 - 1.6 \times 10^6 M_{\odot}$. Supernovae are spread randomly within a sphere of $r_c = 60$ pc, and inject energy episodically with a specific rate $1/130 M_{\odot}^{-1}$ proportional to the star formation rate (SFR) in the cluster. Models are run for several values of SFR in the range 0.01 to 0.1 $M_{\odot} \text{ yr}^{-1}$, with the corresponding average surface energy input rate $\sim 0.04\text{--}0.4 \text{ erg cm}^{-2} \text{ s}^{-1}$. We find that the discrete energy injection by isolated SNe are more efficient in blowing superbubbles: Asymptotically they reach heights of up to 3 to 16 kpc for $M_{cl} = 10^5 - 1.6 \times 10^5 M_{\odot}$, correspondingly, and stay filled with a hot and dilute plasma for at least 30 Myr. During this time, they emit X-ray, H α and dust infrared emission. X-ray luminosities $L_X \propto \text{SFR}^{3/5}$ that we derive here are consistent with observations in star-forming galaxies. Even though dust particles of small sizes $a \leq 0.03 \mu\text{m}$ are sputtered in the interior of bubbles, larger grains still contribute considerably ensuring the bubble luminosity $L_{\text{IR}}/\text{SFR} \sim 5 \times 10^7 L_{\odot} M_{\odot}^{-1} \text{ yr}$. It is shown that the origin of the North Polar Spur in the Milky Way can be connected with activity of a cluster with the stellar mass of $\sim 10^5 M_{\odot}$ and the SFR $\sim 0.1 M_{\odot} \text{ yr}^{-1}$ some 25–30 Myr ago. Extended luminous haloes observed in edge-on galaxies (NGC 891 as an example) can be maintained by disc spread stellar clusters of smaller masses $M_* \lesssim 10^5 M_{\odot}$.

Key words: shock waves – ISM: supernova remnants – galaxies: haloes – galaxies: starburst – infrared: galaxies – X-rays: galaxies.

1 INTRODUCTION

The discovery and intensive study of absorptions from heavy elements (such as CIV, SiIV, NV, OVI) in the circumgalactic medium (CGM) in quasar absorption spectra (e. g. Prochaska et al. 2006; Simcoe et al. 2006; Prochaska et al. 2017) have posed stellar feedback as one of the most important physical factors that determine, along with gravity, the structure and evolution of galaxies. It has become clear that energy and mass exchange between interstellar discs and circumgalactic environments driven by energy released from massive stars and supernovae is ubiquitous among galaxies. Even dwarf galaxies at the low end of the star formation rate (SFR) reveal extended metal polluted haloes around them (Bordoloi et al. 2014; Burchett et al. 2015). More recently, Keeney et al. (2017) reported about the presence of such haloes around galaxies without currently ongoing star formation. This suggests a very efficient mass exchange between galactic discs where heavy elements are produced and their distant neighbourhood in the halo.

A common understanding is that the mass exchange between galaxies and their extragalactic environments is maintained by energy release from an enhanced SF that drives galactic winds. Galactic wind, a large scale gas outflow from star formation in galactic discs,

is thought to be driven by energy injection from young stars and supernovae in starbursts events with a surface SFR exceeding a certain critical value. The threshold for galactic winds driven by central starbursts is estimated of $\dot{\epsilon} \sim 10 \text{ erg cm}^{-2} \text{ s}^{-1}$ (Lehnert & Heckman 1996a; Heckman 2000), and for disc-halo circulation in edge-on galaxies $\dot{\epsilon} \sim 10^{-3} - 10^{-4} \text{ erg cm}^{-2} \text{ s}^{-1}$ (Dahlem, Liesenfeld & Golla 1995; Rossa et al. 2000; Dahlem, Liesenfeld & Rossa 2006). However, study of interrelations between the soft X-ray, UV, H α , FIR, and 1.4 GHz radio continuum emissions in a larger sample of 23 edge-on-galaxies led only to put a lower limit on the surface SN energy input rate $\dot{\epsilon} \geq 10^{-3} \text{ erg cm}^{-2} \text{ s}^{-1}$ (Tüllmann et al. 2006).

From a theoretical point of view, the evaluation of the energy threshold is a challenge. It is obvious that this threshold depends on many factors: Ambient gas density, its vertical stratification – characteristic scale heights and the circumgalactic floor density, concentration of energy sources both in space and time, dark matter (DM) distribution, energy injection regime, and so forth (Rossa et al. 2000; Dahlem et al. 2001; Dahlem et al. 2006; Nath & Shchekinov 2013; Roy et al. 2013; Vasiliev, Nath & Shchekinov 2015; Girichidis et al. 2016; Vasiliev, Shchekinov & Nath 2017; Yadav et al. 2017; Fielding, Quataert & Martizzi 2018; Vasiliev, Shchekinov & Nath 2019). Moreover, circulation of gas between different regions of a vertically stratified interstellar gas requires different characteristic energy input rates. From simulations, the required energy rate for

* E-mail: eugstar@mail.ru

driving low Mach number superbubbles ($M \lesssim 3$) confined to the lower halo layer (within 2–3 scale heights) is $\dot{\epsilon} \sim 10^{-4} \text{ erg cm}^{-2} \text{ s}^{-1}$ (Vasiliev et al. 2017; Yadav et al. 2017; Fielding et al. 2018; Shchekinov 2018; Vasiliev et al. 2019), whereas a transition of gas circulation to the outer halo layers, being comparable in size to the galactic radial scale, seems to occur under shocks with higher Mach numbers ($M \gtrsim 10$) requiring an order of magnitude larger energy rate $\dot{\epsilon} \gtrsim 10^{-3} \text{ erg cm}^{-2} \text{ s}^{-1}$ (Roy et al. 2013). Early observations of our Galaxy towards the central region in 408 GHz have revealed loop-like structures – Loop I amongst the most prominent (Hanbury Brown, Davies & Hazard 1960; Berkhuijsen et al. 1971; Haslam et al. 1983). More detailed analysis of the morphology of Loop I in 408 GHz and X-ray patterns from *ROSAT* led Sofue (1994) to conclude that Loop I is produced by a starburst in the Galactic centre (GC) (radius of ~ 200 pc) with total energy of $E \sim 3 \times 10^{56} \text{ erg}$ within nearly 15 Myr (the equivalent SFR $\sim 2 M_{\odot} \text{ yr}^{-1}$). The corresponding surface energy input rate lies in the range $\dot{\epsilon} \sim 0.2 \text{ erg cm}^{-2} \text{ s}^{-1}$ derived in (Nath & Shchekinov 2013). A more recent numerical analysis has demonstrated that large scale structures similar to Loop I in our Galaxy might require even a higher energy input $\dot{\epsilon} \sim 1 \text{ erg cm}^{-2} \text{ s}^{-1}$ (Sarkar, Nath & Sharma 2015).

The discovery of the Fermi-Bubbles (Dobler et al. 2010; Su, Slatyer & Finkbeiner 2010) has revealed a deficit of the SFR in the GC as compared to the value needed for their maintenance. It was found that the GC shows a modest level of star formation, which is not sufficient for providing the energetics of Loop I (Sofue 1994). The estimates have been confirmed by more accurate evaluation from numerical simulations in Sarkar et al. (2015). Yusef-Zadeh et al. (2009) have inferred the history of SF rate in the GC (400 pc radius) from *Spitzer* and *Midcourse Space Experiment* and concluded that the SF rate during the latest history – the last 10 Myr, is only $\sim 0.04\text{--}0.08 M_{\odot} \text{ yr}^{-1}$, while the SFR averaged over 10 Gyr is $\langle \text{SFR} \rangle \lesssim 0.14 M_{\odot} \text{ yr}^{-1}$. The surface energy input rate is thus $\dot{\epsilon} \sim (2.5\text{--}5) \times 10^{-3} \text{ erg cm}^{-2} \text{ s}^{-1}$ during the last 10 Myr, and $\langle \dot{\epsilon} \rangle \sim 0.01 \text{ erg cm}^{-2} \text{ s}^{-1}$ over 10 Gyr. Even though this number looks consistent with the limits determined in Dahlem et al. (1995), Tüllmann et al. (2006) for galactic discs, and the early estimate by Heckman (2000) for galactic winds, numerical simulations raise the lower limit of the required energy input by a factor of at least 3–5 (Sofue 1994; Sarkar et al. 2015). The inconsistency between the estimated SFR and the very existence of the Fermi-bubbles may be attributed to observational difficulties of inferring star formation rate on long time scales caused by a crowded environment in the Central molecular zone (CMZ), which causes uncertainties in counting stars of different age, measurements of infrared, bremsstrahlung emissions, and other indicators of star formation. More recent discussions (see e.g. Krumholz & Kruijssen 2015; Federrath et al. 2016; Krumholz, Kruijssen & Crocker 2016; Barnes et al. 2017; Kruijssen 2017) suggest that a short-term episodic regime of star formation with less pronounced observational manifestations can be possible.

A similar phenomenon, the existence of extended haloes in galaxies with a relatively weak SF rate in the underlying discs, is observed in several edge-on galaxies in the local Universe. The galaxy NGC 891 represents a good example with the SFR $\approx 4 M_{\odot} \text{ yr}^{-1}$ across the disc (optical radius $R_{25} \sim 20$ kpc) equivalent to $\dot{\epsilon} \sim 10^{-4} \text{ erg cm}^{-2} \text{ s}^{-1}$, and at the same time with a halo extending up to $\sim 2\text{--}5$ kpc in dust IR emission (Howk & Savage 1999; Alton et al. 2000; Rossa et al. 2004; Hughes et al. 2014; Seon et al. 2014; Bocchio et al. 2016; Yoon et al. 2021, see also a recently published catalogue of dusty edge-on galaxies in Shinn 2018), ~ 5 kpc in 2–5 keV (Hodges-Kluck, Bregman & Li 2018), to ~ 10 kpc in soft X-ray

(0.4–1.4 keV), and to ~ 20 kpc in HI (Oosterloo, Fraternali & Sancisi 2007). Extended circumgalactic gas traced by CIV, SiIV, and OVI ions at projected radii of the order of 100 to 200 kpc are observed around galaxies, often with a rather modest SFR $\sim 1\text{--}3 M_{\odot} \text{ yr}^{-1}$ (see discussion in Tumlinson, Thom & Werk 2011; Bordoloi et al. 2014). Such extended haloes can either indicate that even a low SF rate under certain conditions is capable to drive circulation of gas within the inner and outer haloes as in the former case, or they are caused by powerful starbursts that have taken place in the past, e.g. 20–30 Myr ago, as in the latter.

In this paper, we focus on the ability of SF in galactic stellar clusters with a low to modest SFR ($0.02\text{--}0.1 M_{\odot} \text{ yr}^{-1}$) and energy injection concentrated in a relatively small volume to drive outflows between the disc and the halo and on their observational manifestations in X-ray, optical, and far-infrared (FIR) tracers. In Section 2, we describe the model we use in simulations, Section 3 presents the results: (i) evolution of the bubble under the action of a cluster depending on its SFR in Section 3.1, including also (ii) destruction of dust particles in Section 3.1.4, (iii) the bubble emission characteristics – X-ray, dust FIR, and $\text{H}\alpha$, and their possible interrelations in Section 3.2, in Section 4, we consider possible implications of our results for the Milky Way and edge-on galaxies with a focus on NGC 891 among them, Section 5 summarizes the results.

2 MODEL DESCRIPTION

2.1 Equilibrium

We carry out 3D hydrodynamic simulations (Cartesian geometry) of SN explosions inside a massive stellar cluster located in the GC. We study the dynamics of a bubble expanding preferentially perpendicular to the disc. We consider the bubble evolution during a period approximately twice as the lifetime of a least massive SN progenitor with $M \sim 8 M_{\odot}$, i.e. ~ 35 Myr. The gaseous disc is set up to be initially in hydrostatic equilibrium in the gravitational potential of the DM halo and the stellar disc (see e.g. de Avillez 2000; Hill et al. 2012; Walch et al. 2015; Li, Bryan & Ostriker 2017; Vasiliev et al. 2019). The z -component of the gravitational acceleration due to the DM halo is calculated from a Navarro–Frenk–White profile with the virial radius of the halo equal to 200 kpc and concentration parameter $c = 12$.

2.2 Stellar disc

The stellar disc is assumed to be self-gravitating with an isothermal velocity dispersion. The acceleration perpendicular to the disc is $g_*(z) = 2\pi G \Sigma_* \tanh(z/z_*)$, where Σ_* and z_* are the stellar surface density and the scale height of the stellar disc. We adopt $\Sigma_* = 200 M_{\odot} \text{ pc}^{-2}$ and $z_* = 0.3$ kpc.

2.3 Gaseous disc

The gas density in the mid-plane is assumed $n_0 = 0.3 \text{ cm}^{-3}$ following (Kalberla & Kerp 1994), which corresponds to gas surface density $\Sigma_g = 1 M_{\odot} \text{ pc}^{-2}$ with the scale height $z_g = 0.2$ kpc at $R = 1$ kpc. At larger heights above the mid-plane, we assume a warm-hot gaseous halo with the profile $n(z) = n_h [1 + (z/z_h)^2]^{-0.75}$, where $n_h = 0.01 \text{ cm}^{-3}$, $z_h = 0.8$ kpc as follows from the Milky Way halo distribution in Miller & Bregman (2015). The temperature of the gaseous disc is set to 10^4 K, the temperature of the halo increases with height to keep hydrostatic equilibrium. Fig. 1 shows the initial gaseous density profiles in the vertical direction, with $n_h = 0.01 \text{ cm}^{-3}$ as our fiducial

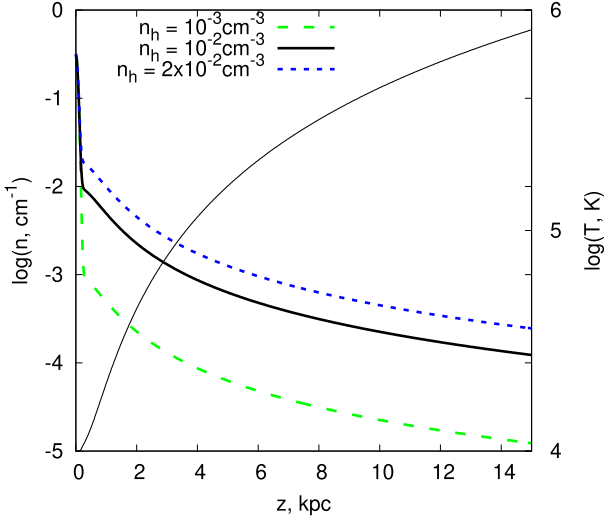


Figure 1. Gas density (left axis, thick lines) and temperature (right axis, thin line) profiles. The halo density is $n_h = 10^{-3}$ (dashed), 10^{-2} (solid), and $2 \times 10^{-2} \text{ cm}^{-3}$ (dotted). The density at the disc mid-plane in all models is $n_d = 0.3 \text{ cm}^{-3}$. The temperature profile is the same for all halo density values.

value. The initial metallicity in disc is assumed to be solar, in the vertical direction the metallicity decreases to its floor value $[Z/H] = -3$ at heights larger than 1 kpc. This allows us to better trace propagation of metallicity from exploded supernovae (SNe) into the halo. Initially the heating rate in the unperturbed disc and halo is set equal to the cooling rate according to the initial values of temperature and metallicity.

2.4 Energy injection

The dominant energy source feeding growing superbubbles is explosions of SNe, with a minor contribution from stellar wind as demonstrated recently by Franeck et al. (2022). We inject the mass and energy by individual events with the energy corresponding to a joint energy of 30 standard SNe. Masses of standard SNe progenitors in a cluster are distributed randomly within 8–40 M_\odot range according to the Salpeter initial mass function, the specific per mass SN rate is $v_m = 1/130 M_\odot^{-1}$. Therefore, each joint injection carries the energy $3 \times 10^{52} \text{ erg}$ in thermal form and the mass load of 240–1200 M_\odot . This allows us to consider larger computational cells and assumes the injection radius corresponding to the Sedov–Taylor solution to be smaller than the cooling length. The energy injection in form of thermal energy seems to be the most suitable in models with randomly spread in space and time point-like sources mimicking discrete SNe. As stressed above, with the chosen cell size, we avoid the overcooling problem discussed in Sharma et al. (2014). The interval between following energy injections corresponds in average to the lifetime of massive stars within 8–40 M_\odot $t_l \sim M^{-1.57}$ (see in Iben 2012). The energy and mass are injected randomly into a cell located within a spherical region of radius 60 pc centred at $(x, y, z) = (0, 0, 0)$. This procedure mimics random SNe explosions in a cluster. Overall, the energy injection rate in each of such clusters corresponds to explosions of standard SNe with the rate $\sim 10^{-4} - 10^{-3}$ SN per year, or equivalently $\text{SFR} \sim 10^{-2} - 0.1 M_\odot \text{ yr}^{-1}$, the corresponding stellar masses of clusters are in the high mass end of the clusters’ mass function $M_{cl} \sim (2-16) \times 10^5 M_\odot$ (Krumholz, McKee & Bland-Hawthorn 2019). Note that $\text{SFR} = 1 M_\odot \text{ yr}^{-1}$ within

the energy injection volume of radius $r_c = 60 \text{ pc}$ corresponds to the surface SN energy injection rate $\epsilon \sim 2.5 \text{ erg cm}^{-2} \text{ s}^{-1}$.

2.5 The code and simulations

The code is based on the unsplit total variation diminishing (TVD) approach that provides high-resolution capturing of shocks and prevents unphysical oscillations. We have implemented the Monotonic Upstream-Centered Scheme for Conservation Laws (MUSCL)-Hancock scheme and the Haarten-Lax-van Leer-Contact (HLLC) method (see e.g. Toro 1999) as an approximate Riemann solver. This code has successfully passed the whole set of tests proposed in Klingenberg, Schmidt & Waagan (2007).

Simulations are run with a radiative cooling described by a set of tabulated non-equilibrium cooling functions calculated by using the approach described in detail (Vasiliev 2013). The functions are obtained for the gas cooling isochorically from 10^8 K down to 10 K for metallicities within the range $[Z/H] = -4.1$. The non-equilibrium calculation (Vasiliev 2011, 2013) includes kinetics of all ionization states of H, He, C, N, O, Ne, Mg, Si, Fe, as well as kinetics of molecular hydrogen at $T < 10^4 \text{ K}$. Fig. A1 in Appendix A presents this set of cooling functions.

We apply a diffuse heating term representing the photoelectric heating of dust grains (Bakes & Tielens 1994), which is thought to be the dominant heating mechanism in the interstellar medium. In our simulations, the heating rate is assumed to be time-independent and exponentially decreasing in the vertical direction with the scale height of the ISM disc. Such an assumption allows to stabilize radiative cooling of ambient gas with the temperature profile shown in Fig. 1. Any deviation of the heating rate in the unperturbed gas violates the balance between cooling and heating and stimulates thermal instability, resulting in the redistribution of gas mass in the interstellar disc (see e.g. in de Avillez 2000; Hill et al. 2012). The heating rate exponentially decreasing upwards across the whole computational domain suppresses such contaminations (Li et al. 2017).

The simulations are performed with a physical cell size of 20 pc. The standard computational domain contains $768 \times 384 \times 768$ cells, which corresponds to $15.36 \times 7.68 \times 15.36 \text{ kpc}^3$, but in several cases, we extend the domain. We suppose a symmetry relative to the disc mid-plane and along the plane going through the cluster centre perpendicular to the mid-plane, so we consider one-fourth of the space. Usually, we restrict our simulations within 35 Myr, at the end of this period, the total vertical momentum of a bubble becomes negative. We complete the simulation earlier if the bubble reaches the borders of the computational domain, even though the total vertical momentum remains highly positive.

3 RESULTS

3.1 Bubble evolution

3.1.1 Gas

In our model the cluster size is comparable to the disc scale height, therefore, the collective bubble formed by SNe with the rate 2×10^{-4} SN per year ($\text{SFR} = 0.026 M_\odot \text{ yr}^{-1}$, $v_{\text{SN}} \simeq 10^{-9} \text{ yr}^{-1} \text{ pc}^{-3}$) considered here as an example, expands preferentially in the vertical direction, and during $\sim 1-2 \text{ Myr}$ reaches heights of $\sim 1-2 \text{ kpc}$. When the shock wave approaches the interface between the disc and the halo at $z \sim 0.5 \text{ kpc}$ (seen in Fig. 1) Rayleigh–Taylor instability

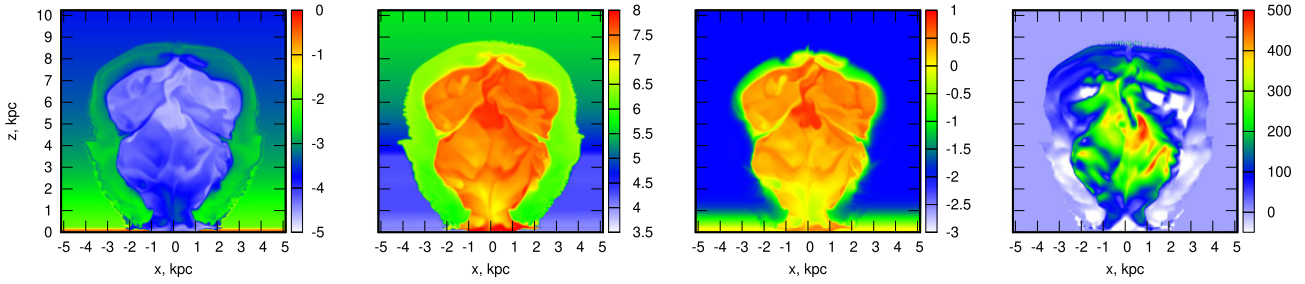


Figure 2. 2D slices showing gas number density ($\log[n, \text{cm}^{-3}]$, first panel), temperature ($\log[T, \text{K}]$, second panel), metallicity ($[Z/H]$, third panel), z -component of velocity ($v_z, \text{km s}^{-1}$, fourth panel) distributions in the outflow formed by SNe explosions in a cluster located at $(x, y, z) = (0, 0, 0)$ with $\text{SFR} = 0.026 \text{ M}_\odot \text{ yr}^{-1}$ ($v_{\text{SN}} \simeq 10^{-9} \text{ yr}^{-1} \text{ pc}^{-3}$). The bubble age is 25 Myr. The halo profile is fiducial with central density $n_h = 10^{-2} \text{ cm}^{-3}$.

breaks the shell and hot gas expands into halo with a larger scale height, resulting in a bottle-neck shaped bubble. At age ~ 15 Myr SNe explosions exhaust and the bubble continues expansion under momentum conservation.

Fig. 2 presents the hydrodynamical field in the outflow formed by the cluster at the age 25 Myr – left to right: gas density, temperature, metallicity, z -component of velocity. The bubble reaches almost 9 kpc in height and about 8 kpc in its widest part. The bubble shell is still thick, around 1 kpc, and hot, $T \gtrsim 10^6 \text{ K}$. Effects of radiative cooling are marginally observed in the lowermost region of the bubble edge in form of a small-scale density enhancement. The bubble interior is hotter than its shell – $T \gtrsim 10^7 \text{ K}$ and will remain as hot further on for a characteristic cooling time $t_c \sim 30\text{--}100 \text{ Myr}$. The bubble is still expanding with velocity $\gtrsim 100 \text{ km s}^{-1}$, and with positive velocities dominating almost in the entire bubble, except in the outer regions of the hot interior at heights $z \sim 6 \text{ kpc}$ and the compressed shell below $\sim 4 \text{ kpc}$.

3.1.2 Metals

Metals ejected by SNe partly mix with the ambient hot bubble gas resulting in the metallicity spread from $[Z/H] = 0$ to $[Z/H] = 1$. It is worth to be pointed out that in our model mixing operates due to numerical diffusion $D_n \sim c_s \Delta x / 3 \sim 2 \times 10^{26} \text{ cm}^2 \text{ s}^{-1}$ in the shell with sound speed $c_s \sim 100 \text{ km s}^{-1}$, and $\sim 10^{27} \text{ cm}^2 \text{ s}^{-1}$ in the hot bubble with $c_s \sim 500 \text{ km s}^{-1}$. This is consistent with the estimate of numerical kinematic viscosity $\langle \eta_n \rangle$ corresponding to the increase of specific per mass thermal energy u as if it was grown due to viscosity at shock fronts ($\eta_n \sim \langle \dot{u} / (\nabla \cdot \mathbf{v}) \rangle$). Within $\sim 25 \text{ Myr}$ numerical diffusion can mix metallicity over $\sqrt{\langle \Delta x^2 \rangle} \sim 600 \text{ pc}$ which is half of the shell thickness. In the bubble interior, mixing covers $\sim 3 \text{ kpc}$ in the same time range. In the thin external interface at the uppermost parts of the contact discontinuity it remains lower than $[Z/H] = -1$, indicating that mixing between the ejecta and ambient gas is slow. Inefficient mixing is one of the reasons that the shell is hot, the cooling time in shell with $[Z/H] = -1$ is of the order 30–50 Myr. It is worth also noting that metals do not penetrate into the very external layer of the shell of $\sim 3 \text{ kpc}$, being confined in a thinner layer $\sim 0.5\text{--}1 \text{ kpc}$ – it can be seen when comparing the distributions of metals and temperature/density on Fig. 2. It is also seen that in the lower (conical) parts of the shell metals remain locked in even a thinner layer of $\sim 0.1\text{--}0.2 \text{ kpc}$ because of a lower temperature and higher density in this domain. At the asymptotic (‘inertial’) stage with exhausted SNe explosions shown in Fig. 2 metals are swept up from the superbubble centre, as can be observed in the central domain deficient in metals.

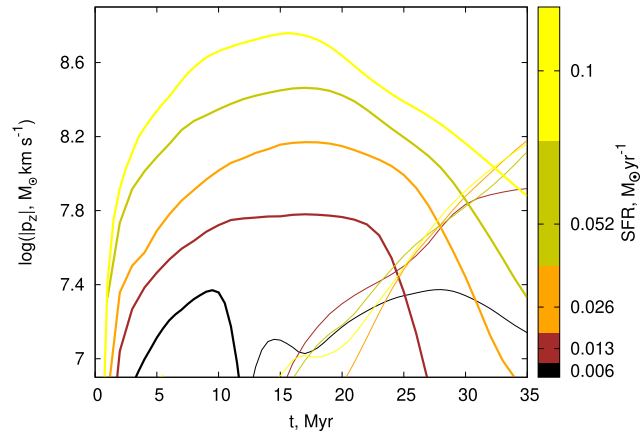


Figure 3. The z -component of momentum for outflowing ($p_z > 0$, thick lines) and infalling ($p_z < 0$, thin lines) gas flows for models with $\text{SFR} = 0.006, 0.013, 0.026, 0.052, \text{ and } 0.1 \text{ M}_\odot \text{ yr}^{-1}$.

3.1.3 Overall dynamics

Long-term evolution of superbubbles can be illustrated by time-behaviour of their vertical momentum $p_z = \int \rho v_z dV$ shown in Fig. 3 for several bubble models. Typically fast growth of $p_z(t)$ at very initial stages changes to a slow continuous gain on longer times $\sim 5\text{--}10 \text{ Myr}$ until reaching the maximum of p_z . For lower SFR, except the lowest with the $\text{SFR} = 0.006 \text{ M}_\odot \text{ yr}^{-1}$, the maximum stays on a plateau for long times (up to 15 Myr for $\text{SFR} = 0.013 \text{ M}_\odot \text{ yr}^{-1}$). On the contrary, superbubbles from clusters with higher SFR pass the maximum phase faster. The maximum and following drop of p_z are connected mostly with a decrease of the shell mass because of a downward slipping of cold gas fragments along the shell. This can be the result of an enhanced pressure under more energetic shock waves from clusters with higher SFR, which stimulate faster gas cooling and the corresponding depletion of the shell mass. This process limits the expansion of shells. The superbubble from the minimum $\text{SFR} = 0.006 \text{ M}_\odot \text{ yr}^{-1}$ is an exception of this trend: The shell with such a low SFR expands on average into a denser environment than it gains for larger superbubbles, and its gas cools faster than gains energy from feeding explosions. The expansion phase ends by freezing out of the shells (Fig. 4), until they are disrupted by turbulence, by ongoing star formation nearby and/or galactic differential rotation. Depending on the SFR in the parent cluster it may take next tens of Myr as seen in Fig. 4.

The model with $\text{SFR} = 0.006 \text{ M}_\odot \text{ yr}^{-1}$ seems to be close to the threshold SFR capable to drive the superbubbles. Very rough estimates based on a comparison of the ram pressure from exploding SNe

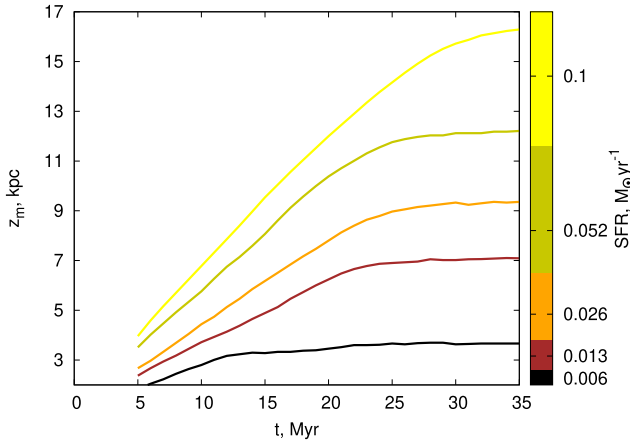


Figure 4. The height of a bubble versus the age for SFR = 0.006, 0.013, 0.026, 0.052, and 0.1 $M_{\odot} \text{ yr}^{-1}$.

$L/4\pi z^2 v_s$ on the shell of radius $R_s \sim z$, and the disc gravity $\rho_{sh} g_* z$, result in

$$L \sim \pi \rho_{sh} g_* z^3 v_s \sim 7.5 \times 10^{41} n z_3^3 v_{100} \text{ erg s}^{-1}, \quad (1)$$

for the disc parameters as in Section 2.2. Here, $L \sim v_{sn} E_B$ is the mechanical luminosity of exploding SNe, v_s , the shell velocity $v_{100} v_s / (100 \text{ km s}^{-1})$. The shell expansion velocity in the segments with predominantly vertical walls $v_{100} \lesssim 0.3$, $z_3 = z/3z_*$, and g_* estimated at $z \lesssim 3z_*$. With these assumptions equation (1) is equivalent to the SFR $\sim n z_3^3 v_{100} M_{\odot} \text{ yr}^{-1}$, or SFR $\sim 0.001 M_{\odot} \text{ yr}^{-1}$ for $n \sim 10^{-3} \text{ cm}^{-3}$, $z = 3z_* \sim 3 \text{ kpc}$, and $v_s \sim 100 \text{ km s}^{-1}$. It is important to stress though, that this conclusion is valid for star-formation localized in clusters with characteristic radius $R_c \sim 40 \text{ pc}$, immersed into ambient gas with the parameters close to those defined in Section 2.3.

Fig. 5 presents the outer borders (defined by the density jump) of the superbubbles evolving to this asymptotic: From left to right, we show the bubbles driven by clusters with SFR = 0.006, 0.013, 0.026, 0.052, and 0.1 $M_{\odot} \text{ yr}^{-1}$ at several epochs. Nearly equidistant contours during the first 20 Myr show that the bubbles grow uniformly, i.e. with a constant velocity. After this period the bubbles driven by SFR $\sim 0.006\text{--}0.05 M_{\odot} \text{ yr}^{-1}$ start decelerating until their vertical expansion terminates by $t \sim 20\text{--}25 \text{ Myr}$; the corresponding energy injection rate $\dot{\epsilon} \sim 0.0013\text{--}0.12 \text{ erg cm}^{-2} \text{ s}^{-1}$. Bubbles of higher SF rates end their vertical expansion at later times. Radial expansion lasts several Myr shorter. The smallest superbubble in the first panel expands obviously slower as compared to those with a higher SFR. Moreover, so far as in this case a considerable fraction of the superbubble expands into on average denser medium, the effects of radiative cooling in the walls below $z \lesssim z_h$, and the predominance of negative momentum from these regions, determine a fast decrease of the z -momentum component on Fig. 3.

The superbubble collimation increases with the halo gas density, as seen on two panels of Fig. 6, because a higher density beyond the interface between the ISM disc and the halo suppresses the radial expansion.

3.1.4 Dust destruction

Collisions of heavy ions of energies $E \gtrsim 30 \text{ eV}$ with dust particles result in their sputtering (Burke 1974; Draine 1981; Dwek 1981; Dwek & Arendt 1992). The characteristic sputtering time in a

given computational cell is approximated as $t_d(T) = a |da/dt|^{-1} \approx 10^5 (1 + T_6^{-3}) a_{0.1} n^{-1} \text{ yr}$ ($T \gtrsim 10^6 \text{ K}$, see equation (25.14) in Draine 2011). In a magnetic free medium a non-thermal sputtering proceeds during the motion of a dust particle relative to plasma in a thin layer immediately behind the shock front $\Delta l \sim 10\text{--}20 \text{ pc}$ for the accepted parameters and thus can be neglected in our calculations. Thermal sputtering proceeds for the radiative cooling time $t_r \sim 10^5 T_6 n^{-1} \text{ yr}$ unless local plasma is heated under the action of a shock from a distant SN. A rough estimate of time lags between two subsequent shocks impinging a given point in the bubble is $t_s \sim \bar{v}_{sn}^{-1}$ varying from 2.5×10^2 to $2 \times 10^3 \text{ yr}$ depending on the SFR, here $\bar{v}_{sn} = \int v_{SN} dV$ is the total SNR in the cluster centre. Such a high impinging rate prevents gas cooling and provides a continuous maintenance of high temperature. In this environment, a dust grain loses around 90 per cent of its radius in $t = 2t_d(T)$, and hence in order to account dust destruction in a computational cell at a given stage the condition $t_d(T) \leq t_d$, with t_d being the dynamical time, can be roughly accepted. Therefore, as this condition is met, dust particles with radius a are removed from a given computational cell. Fig. 7 presents the logarithm of the ratio $t_d(T)/t_d$ within the superbubble at different times for a set of particle radii.

As readily seen, smaller particles are sputtered first. However, the contribution of small grains to the thermal emission can remain considerable, particularly at higher frequencies because dust temperature T_d is normally higher for smaller particles. In order to estimate this effect, we plot¹ a distribution of the ratio $t_d(T)/t_d$ in the bubble over its evolution in Fig. 7. It is seen that during the whole evolution, only small dust particles $a < 300 \text{ \AA}$ in the bubble shell are destroyed. In the low-density bubble interior the sputtering time is higher than $\sim 30\text{--}100 \text{ Myr}$ (Dwek & Arendt 1992), such that even small particles partly survive. Accounting for the fact that the shell sweeps up mostly the halo gas with a low dust mass fraction, the effects of dust destruction to the IR emission is of minor importance.

Destruction of dust behind shock fronts is partly replenished by stellar activity via SNe factories (Todini & Ferrara 2001; Bianchi & Schneider 2007; Matsuura et al. 2011; Gall et al. 2014; Lau et al. 2015). We assume that besides the dust already present in the ISM gas, an additional dust mass is supplied into the bubble interior proportionally to the mass of ejected metals by SNe. Collisional heating (Burke 1974; Draine 1981; Dwek 1981; Dwek & Arendt 1992) and destruction (Jones et al. 1994; Tielens et al. 1994; Draine & Salpeter 1979) of the ejected dust is also implemented into our calculations.

3.2 Bubble emission

3.2.1 X-rays

Although radiative losses are too weak to affect the dynamics of the bubble during its expansion, the hot plasma in the interior emits sufficient energy in far-UV and X-ray ranges to manifest observationally. Fig. 8 presents the simulated X-ray emission (in log scale) of a bubble seen edge-on (yz -plane) at $t = 25 \text{ Myr}$, SFR = 0.026 $M_{\odot} \text{ yr}^{-1}$. As seen, X-ray surface intensity of the bubble in the low-energy bands (0.2–0.6 and 0.6–1.0 keV) is considerable ($\sim 3 \text{ keV s}^{-1} \text{ cm}^{-2} \text{ sr}^{-1}$) and comparable to that observed by eROSITA in the Galactic bubbles (see below in Section 4.1), and an order of magnitude lower than

¹We consider five bins of dust with radius 30, 100, 300, 1000 and 3000 \AA following to the ‘standard’ Mathis-Rumple-Nordsieck (MRN) distribution $n_a \propto a^{-3.5}$ (Mathis, Ruml & Nordsieck 1977).

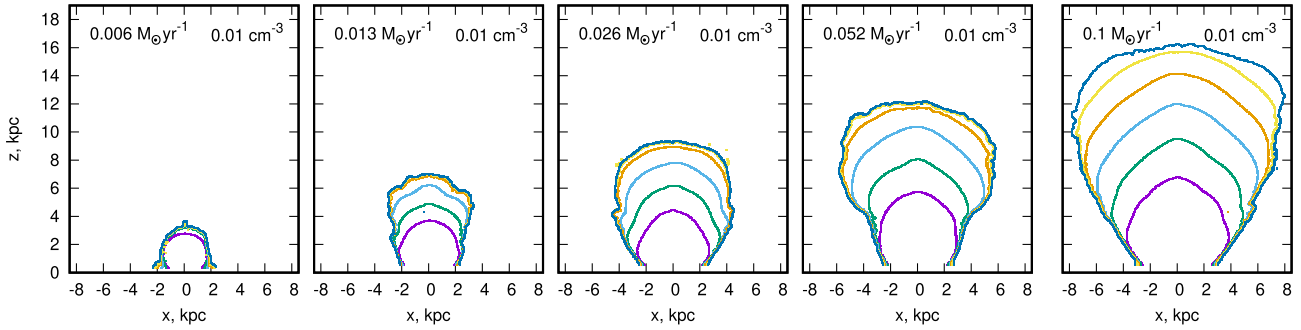


Figure 5. Left to right shown are contours of evolving bubbles with the SFR = 0.006, 0.013, 0.026, 0.052, and $0.1 M_{\odot} \text{ yr}^{-1}$. Contours depict the outer bubbles’ edges at 10, 15, 20, 25, 30, and 35 Myr (from bottom to top). The halo profile is fiducial with $n_h = 10^{-2} \text{ cm}^{-3}$.

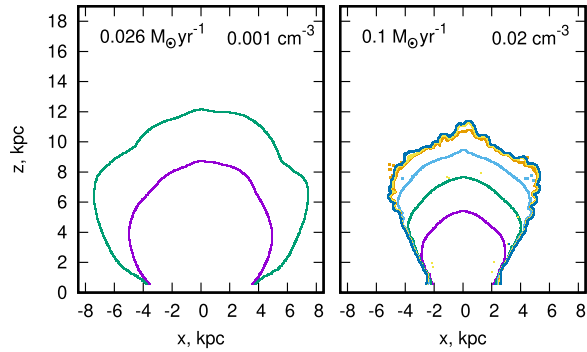


Figure 6. The two panels correspond to clusters with SFR = $0.026 M_{\odot} \text{ yr}^{-1}$ (left) and $0.1 M_{\odot} \text{ yr}^{-1}$ (right) immersed into a low ($n_h = 10^{-3} \text{ cm}^{-3}$) and a high halo density ($n_h = 2 \times 10^{-2} \text{ cm}^{-3}$), respectively.

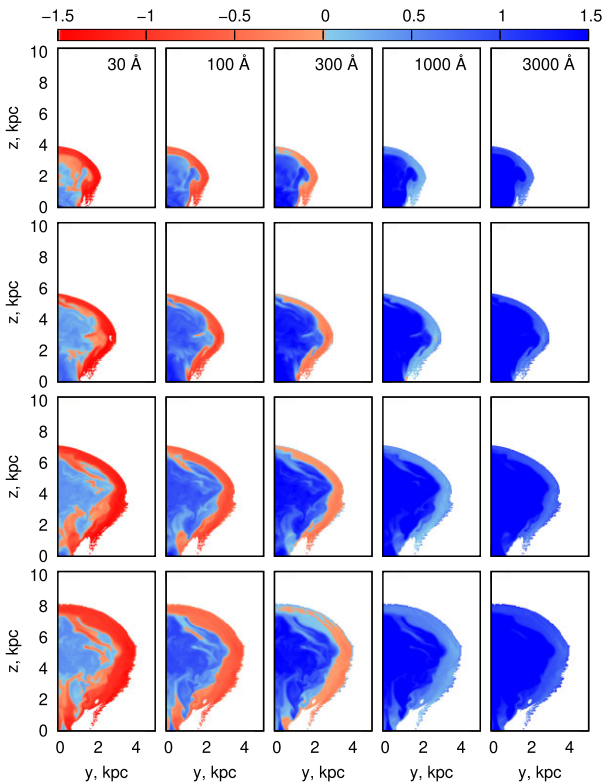


Figure 7. Distribution of the logarithm of the ratio $t_d(T)/t_d$: left to right $a = 30, 100, 300, 1000,$ and 3000 \AA . From top to bottom panels correspond to ages 10, 15, 20, 25 Myr.

the intensity of the diffuse X-ray emission in the halo of NGC 891 galaxy (Temple, Raychaudhury & Stevens 2005). It degrades slowly and stays approximately in the same range of intensity as shown in Fig. 8 within next $\sim 30\text{--}40$ Myr, even after 25 Myr when SNe explosions exhaust. In general, the intensity is more or less uniform throughout the bubble except several large-scale fluctuations in the highest energy bands close to the bubble border at heights $z \sim 2\text{--}8$ kpc.

A slow cooling in the bubble interior keeps the gas hot and the total X-ray luminosity at a sufficiently high level. This is clearly seen in Fig. 9, where evolution of X-ray luminosity in the low energy band $0.5\text{--}2$ keV is shown. The luminosity in this band decreases gradually roughly as $L_X \sim t^{-1/4}$.

The total X-ray luminosity in the $0.5\text{--}2$ keV band from the entire bubble increases for higher SFR approximately as $L_X \propto \text{SFR}^{4/3}$ for $\text{SFR} \lesssim 0.06 M_{\odot} \text{ yr}^{-1}$ and flattens to $L_X \propto \text{SFR}^{1/4} M_{\odot} \text{ yr}^{-1}$ at higher SFR (Fig. 10). The flatness may be caused by the fact that for bubbles with $\text{SFR} \lesssim 0.06 M_{\odot} \text{ yr}^{-1}$, a higher fraction of the hot interior expands adiabatically. The ‘ $L_X\text{--SFR}$ ’ dependence in Fig. 10 is consistent with the integrated ‘ $L_X\text{--SFR}$ ’ relation ($E = 0.3\text{--}2.0$ keV) for star-forming late-type edge-on galaxies (Tüllmann et al. 2006; Li et al. 2017).

3.2.2 IR dust emission

In order to evaluate the influence of dust destruction on their spectrum, we calculate the dust emissivity with and without (depending on their lifetime) small dust grains – we refer the latter ‘burnt’ dust. The left-hand panel in Fig. 11 presents the total IR flux (in log scale) produced by dust with sizes $a \sim 3 \times 10^{-3} - 0.3 \mu\text{m}$ as if it was not destroyed in the entire bubble for the same model and age depicted in Figs 2 and 8. The flux of the dust emission in the right-hand panel of Fig. 11 includes only grains with radii a whose lifetime scale $t_d(T) \geq t_d$ as shown in lowest row Fig. 7. In other words, in the bubble shell it mainly corresponds to the sum of contributions from dust particles $a = 0.03 \dots 0.3 \mu\text{m}$ as shown in the lowest row of Fig. 7. One can see that the smallest grains (30 \AA) give a dim shell-like structure around a smooth bubble from larger grains at the level $\sim 3 \times 10^{-6} \text{ erg s}^{-1} \text{ cm}^{-2}$. Reduced FIR intensity in the shell on the right-hand panel of Fig. 11 is obviously due to a deficient short wavelength emission from small-size particles. One can think that gas in the shells passed through hot and dense stages and destroyed small dust grains should manifest ‘colder’ FIR spectra shifted towards longer wavelengths in comparison with those regions with ‘normal’ dust size content, as seen on the right-hand panel in Fig. 11. It is worth noting that even though sputtering of larger particles partly

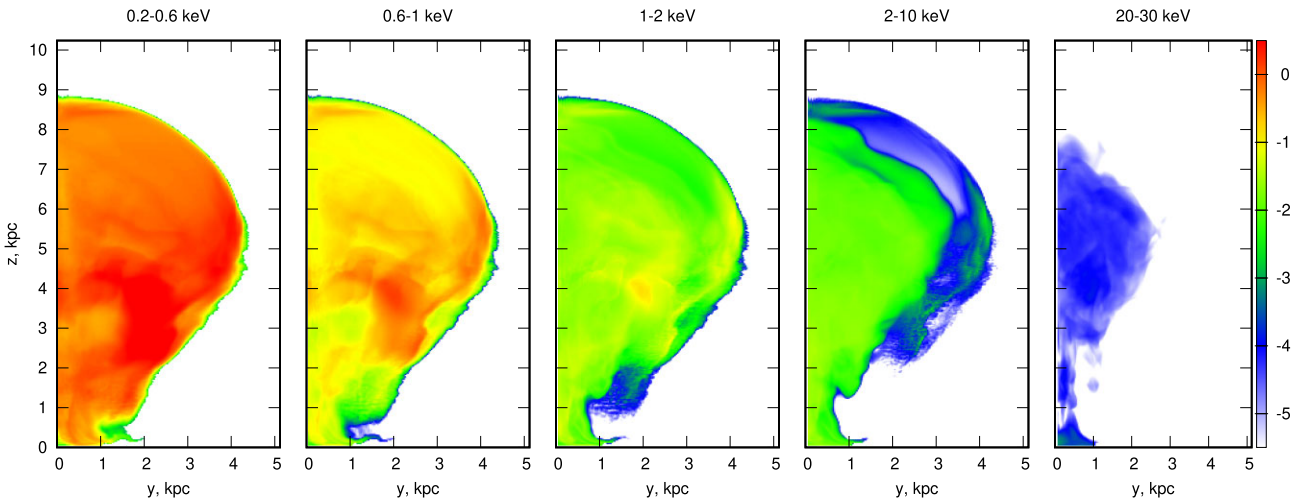


Figure 8. Edge-on (yz -plane) maps of the logarithm of X-ray surface intensity ($\text{keV s}^{-1} \text{cm}^{-2} \text{sr}^{-1}$) in energy ranges 0.2–0.6, 0.6–1, 1–2, 2–10, and 20–30 keV (left to right) for the model with $\text{SFR} = 0.026 M_{\odot} \text{yr}^{-1}$ at the 25 Myr; the halo profile is fiducial: $n_h = 10^{-2} \text{cm}^{-3}$.

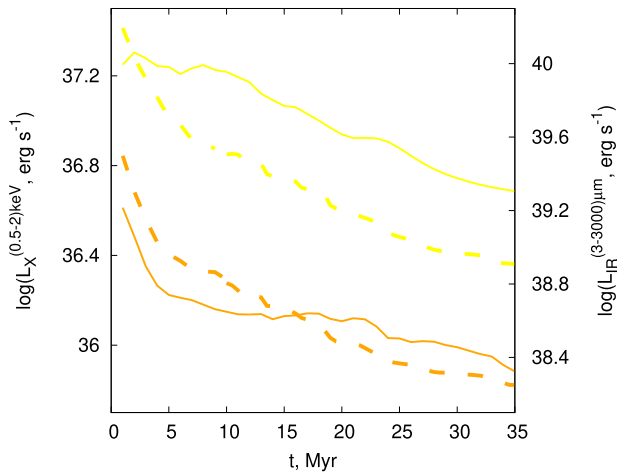


Figure 9. X-ray luminosity in energy range 0.5–2 keV (thin solid lines, left axis) and IR luminosity (thick dashed lines, right axis) from the whole bubble formed by $\text{SFR} = 0.026 M_{\odot} \text{yr}^{-1}$ (two lower orange lines) and $0.1 M_{\odot} \text{yr}^{-1}$ (two upper yellow lines).

replenishes particles of smaller size, it is insufficient to compensate for their loss: First, because the sputtering time-scales with radius $t_a \propto a$, and second, the number of larger particles is smaller, as for instance, in the case of $n_a \propto a^{-3.5}$ spectrum. Larger grains survive longer, as illustrated in Appendix B.

As mentioned above, smaller particles have higher temperature and can contribute predominantly in emission spectra at higher frequencies. The latter is because that even in steady-state conditions dust temperature varies nearly as $T_d \propto a^{-1(4+\beta)}$ ($\beta \simeq 2$ is the dust spectral index), whereas in hot dilute plasma stochastic heating from electrons makes small dust grains even ‘hotter’ than at steady-state conditions (Dwek 1981, 1986): Small dust particles experience higher magnitude of temperature fluctuations around a median value. At such circumstances, an ensemble of dust particles immersed in a hot environment show a thermal spectrum enhanced in the high frequency range. On the contrary, their deficit manifests a modified blackbody spectrum with a monotonic 2nd derivative over frequency, as depicted by the dashed curve in Fig. 12. Observationally, this difference can be obviously recognized on ‘colour’ maps: The maps

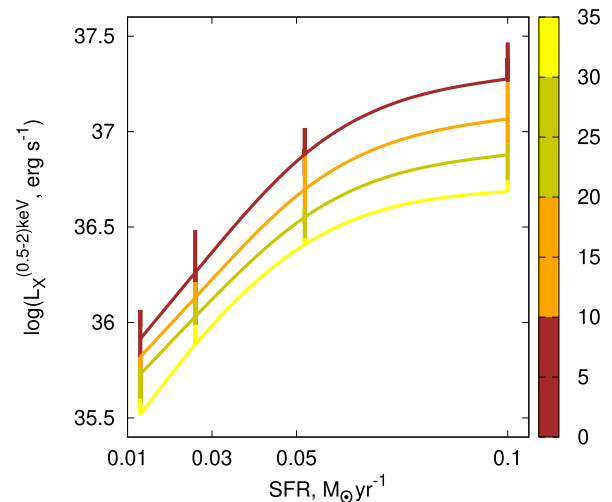


Figure 10. X-ray luminosity in energy range 0.5–2 keV from the whole bubble driven by SFR at 5, 15, 25, and 35 Myr (spline-smoothed lines from top to bottom). The vertical lines show evolution of L_X for a given SFR value. The colour bar encodes time in Myr.

of the ratio $F_{\lambda}(25 \mu\text{m})/F_{\lambda}(250 \mu\text{m})$ – the ratio of intensities at the wavelengths marked in Fig. 12 by yellow bands at which the contribution of small dust into the IR spectrum is clearly distinct. These maps for ‘normal’ and ‘burnt’ dust are shown on the left and right-hand panels in Fig. 13, correspondingly. The bubble with ‘burnt’ dust is obviously seen to suffer of a deficit of emission at short wavelength as compared with the spectrum of an identical bubble with ‘normal’ dust. The difference between the spectrum with a ‘burnt’ and a ‘normal’ dust can be also recognized in a correlation between the dust FIR colour, the ratio $F_{\lambda}(25 \mu\text{m})/F_{\lambda}(250 \mu\text{m})$ and the X-ray intensity. This correlation can be seen in the distribution function of the colour over the superbubble edge-on projection as shown in Fig. 14: The ‘burnt’ dust lacking of small size grains does not show the excess of emission at shorter wavelengths $\lambda < 100 \mu\text{m}$, and thus has a lower ratio $F_{\lambda}(25 \mu\text{m})/F_{\lambda}(250 \mu\text{m}) \lesssim 0.5$, while the ‘normal’ dust shows a higher ratio > 0.7 .

Scatter plots in Fig. 15 show the interrelation between the IR and X-ray surface intensities in different energy ranges for a bubble

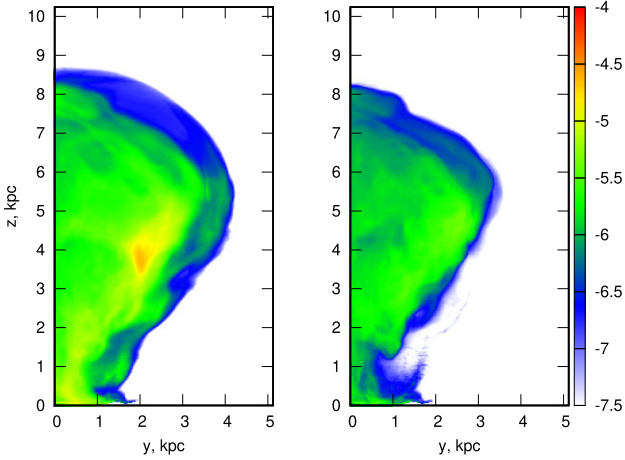


Figure 11. The logarithm of the IR flux (in $\text{erg cm}^{-2} \text{s}^{-1}$) from the dust immersed in the hot bubble: left-hand panel – ‘normal’ dust size spectrum with $n_a \propto a^{-3.5}$ in the range $3 \times 10^{-3} - 0.3 \mu\text{m}$ (dust is assumed to survive against sputtering), right-hand panel shows the case for ‘burnt’ dust predominantly with radii $0.03 - 0.3 \mu\text{m}$ (presented by the sum of contributions from dust shown in the lower row in Fig. 7), SFR = $0.026 M_\odot \text{yr}^{-1}$, the bubble age is 25 Myr.

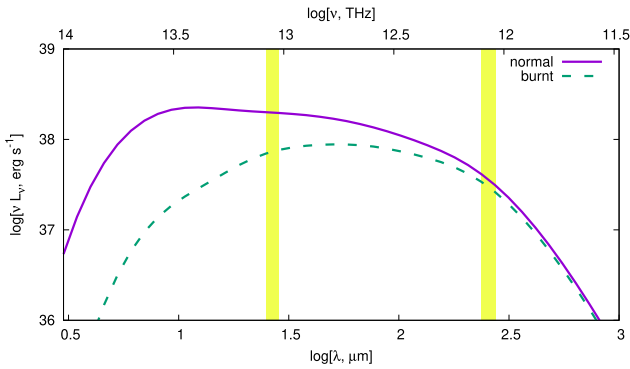


Figure 12. IR emission spectra of dust with ‘normal’ and ‘burnt’ dust composition: solid line represent the left-hand panel of Fig. 11 with ‘normal’ dust, dashed line shows the spectrum of ‘burnt’ dust (in the right-hand panel of Fig. 11), the total (over the covered range) emission in the spectra relate as 0.35. The curves show the spectra *integrated* over all lines of sight in the entire bubble surface field, and thus represent the average spectrum.

fed by $\text{SFR} = 0.026 M_\odot \text{yr}^{-1}$. A remarkable difference between IR distributions of ‘normal’ and ‘burnt’ dust composition is that the former lies at the high intensity end $\gtrsim 3 \times 10^{-6} \text{erg s}^{-1} \text{cm}^{-2}$, whereas the latter tends to lower intensity due to a deficit of small grains (see discussion in Section 3.2.2). The ‘burnt’ dust deficient of smaller grains locates predominantly in the shell and in the edge layer between the shell and the hot bubble, i.e. it is connected spatially with denser and colder plasma. As a result, low-brightness dust emission is present on panels with low-energy X-ray bands, as they occupy the entire field of the bubble, including the dense shell and the edge between the shell and the hot bubble. The energy band $E = 2-10 \text{keV}$ represents the bubble hot interior and its colder shell (Fig. 8). This is reflected in the low-brightness tail both in X-ray and IR. The highest energy band emission ($E = 20-30 \text{keV}$) concentrates towards the bubble centre and has the lowest brightness. The dust in this region mostly avoids destruction from the hostile environment and is, on average, brighter.

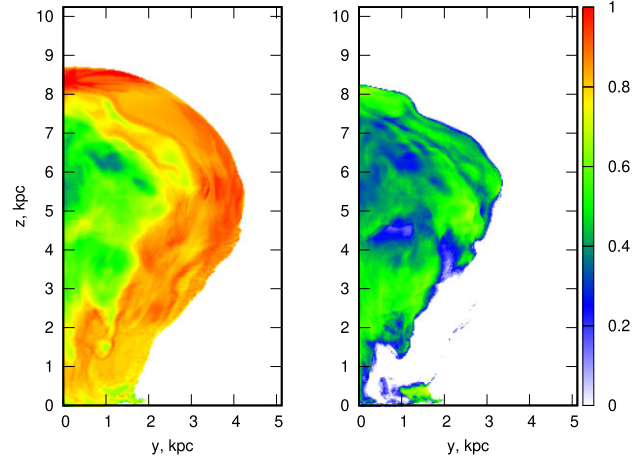


Figure 13. The maps of distributions of the fluxes ratio (in log scale) of $F(25 \mu\text{m})$ to $F(250 \mu\text{m})$ in the bands shadowed yellow in Fig. 12. *Left* and *right*-hand panels reflect the ‘normal’ and ‘burnt’ dust as in Fig. 11.

One can note similar behaviour of the X-ray brightness in the 0.5–2 keV band (third panel in Fig. 15) and the IR surface brightness (fifth panel). As mentioned early, the total X-ray and dust IR luminosities also demonstrate similarity in time dependence: They both decay as $L_{\text{IR}} \sim L_X(0.5 - 2 \text{keV}) \sim t^{-1/4}$ (Fig. 9).

3.2.3 Emissions versus height

Emission characteristics of the superbubble interior depend on gas density and temperature, and therefore, change in height and time. Thus, they can characterize the bubble physical state and the age. Fig. 16 presents emission intensities along the vertical axis averaged over rings centred at $(x = 0, y = 0)$ for a given z -coordinate within radial direction $r = (x^2 + y^2)^{1/2} = 100 \text{pc}$. These are: $\text{H}\alpha$ line, X-ray low-energy (0.6–1 keV), and $\lambda = 3 \mu\text{m}$ to $\lambda = 3 \text{mm}$ IR from dust, commonly used for diagnostics of gaseous haloes in edge-on galaxies.

As can be seen, $\text{H}\alpha$ emission extends at a detectable limit $\gtrsim 10^{-19} \text{erg s}^{-1} \text{cm}^{-2} \text{arcsec}^{-2}$ up to $z \sim 2 \text{kpc}$ indicating that it comes from the lowest parts of the bubbles shells with relatively high densities. X-ray low-energy band with small (within factor of 2) variations occupies the entire superbubble volume (as seen in Fig. 8) and decreases in time. IR dust emission is clearly seen to evolve similar to the low-energy X-ray emission. This reflects the fact that dust easily survives in the hot and X-ray bright bubbles’ interior, as seen from comparison of Fig. 11 with Fig. 8 (the first 3 panels).

OVI ions are known to be very sensitive to temperature variations in a cooling plasma (Vasiliev 2011, 2013) and does not show a clear trend in the vertical distribution. However, it shows a rather intense 1036\AA line emission with $\lesssim 10^{-18} \text{erg cm}^{-1} \text{s}^{-1} \text{arcmin}^{-2}$ and can trace outflows of hot enriched gas into galactic haloes.

4 IMPLICATIONS: MILKY WAY AND NGC 891

4.1 The giant bubble in the galaxy

Estimates of SFR in the central Milky Way during recent 10 Myr vary around $\sim 0.04-0.08 M_\odot \text{yr}^{-1}$ (Yusef-Zadeh et al. 2009; Immer et al. 2012; Koepferl et al. 2015; Barnes et al. 2017) with the corresponding cluster mass of $M \sim 10^4-10^5 M_\odot$, and as such can work as a source for keeping the central superbubble manifested in form of the North

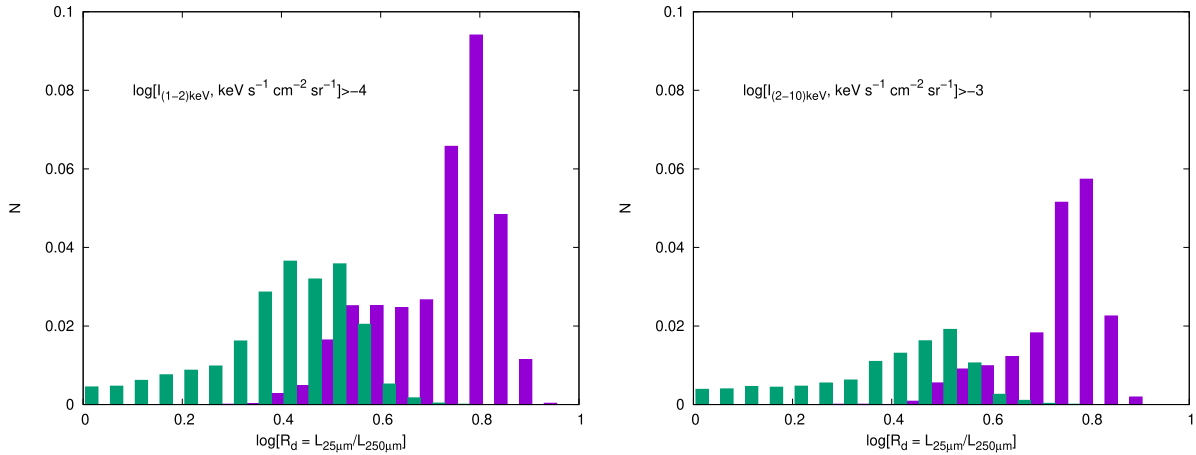


Figure 14. *Left and right-hand panels:* Distributions of ‘colours’ $25 \mu\text{m}/250 \mu\text{m}$ for a superbubble around the cluster with $\text{SFR} = 0.026 M_{\odot} \text{yr}^{-1}$ in regions radiating in the low $E = 1\text{--}2 \text{ keV}$ and high $E = 2\text{--}10 \text{ keV}$ energy bands. Magenta corresponds to a ‘normal’, while green to a ‘burnt’ dust.

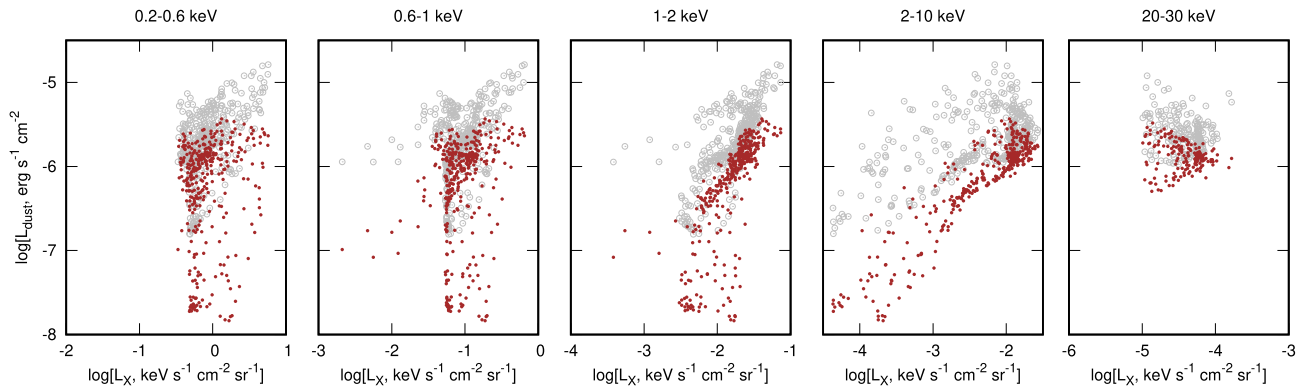


Figure 15. The interrelation between IR surface luminosity dust grains and X-ray intensity in energy bands 0.2–0.6, 0.6–1, 1–2, 2–10, and 20–30 keV (left to right) for model with $\text{SFR} = 0.026 M_{\odot} \text{yr}^{-1}$. Large open (grey) circles present dust grains with ‘normal’ dust-size composition $a = 3 \times 10^{-3} - 0.3 \mu\text{m}$ (presented on the left-hand panel of Fig. 11), whereas small (dark red) dots correspond to the ‘burnt’ particles with a narrower range of dust size-spectrum $a = 10^{-2} - 0.3 \mu\text{m}$ (shown on the right-hand panel of Fig. 11). As seen, differences between the fluxes from ‘normal’ and ‘burnt’ dust is more than an order of magnitude in contrast to shown in Fig. 12, as mentioned, this is because the spectra in Fig. 12 are averaged over the entire volume of the bubbles.

Polar Spur and Fermi-Bubbles. Recently, the eROSITA telescope installed onboard of the Spektr-RG mission has found observational evidence of energy injection into the halo from past activity in the central part of the Milky Way (Predehl et al. 2020). In the 0.6–1.0 keV band, the average observed X-ray intensity within the northern and southern bubbles is around $\sim(2\text{--}4) \times 10^{-15} \text{ erg s}^{-1} \text{ cm}^{-2} \text{ arcmin}^{-2}$.

In our simulations, we consider the evolutionary and emitting properties of similar giant bubbles formed by $\text{SFR} = 0.013\text{--}0.1 M_{\odot} \text{yr}^{-1}$ (Fig. 5). The intensity obtained in our models is close to that observed in the Galaxy. The bubble from a cluster with the $\text{SFR} = 0.1 M_{\odot} \text{yr}^{-1}$ reaches the height $\approx 14 \text{ kpc}$ at 25 Myr (fourth panel on Fig. 5), that is close to the observed height of the North Polar Spur. For an observer at 8 kpc from the centre, the X-ray intensity (in 0.7–1.2 keV) of the bubble in galactic coordinates is shown in Fig. 17. The intensity in the bright shell is close to the values detected by eROSITA: $\sim(1\text{--}3) \text{ keV s}^{-1} \text{ cm}^{-2} \text{ sr}^{-1}$. As can be seen from Fig. 4 at $t = 25 \text{ Myr}$, the bubble continues to expand. In the next 10 Myr, its flux decreases by a factor of $\sim 1.2\text{--}1.5$, and the shell rises up to latitudes of 80° . The overall morphology is similar to the Milky Way bubble. Small-scale morphological differences are observed at lower latitudes, where details of inhomogeneous distribution of gas

and star formation around the central galactic zone can introduce peculiarities into dynamics.

Sarkar et al. (2015) have described first a 2D dynamical model of a galactic scale outflow that might have resulted in the formation of the Loop I structure and Fermi-bubbles inside. The overall dynamics are very similar to ours, with small differences in morphology, which are connected with the difference in energy injection regimes: Spherically symmetric wind with a continuous rate in their model versus episodic explosions from individual SNe randomly spread in space and time within a central spherical stellar cluster of radius $r_c = 60 \text{ pc}$. The effective luminosities though differ by a factor of five: Star formation rates $0.5 M_{\odot} \text{yr}^{-1}$ in Sarkar et al. (2015) model versus $0.1 M_{\odot} \text{yr}^{-1}$ in our most powerful model with the SFR close to the observed one (Yusef-Zadeh et al. 2009; Immer et al. 2012; Koepferl et al. 2015; Barnes et al. 2017). The difference is also in the total activity of the central source: Sarkar et al. (2015) considered the central source active for over 27 Myr, whereas in our case the star formation ceased at $t \sim 15 \text{ Myr}$. The superbubble vertical scales are similar though: $\sim 15 \text{ kpc}$ at $t \sim 25\text{--}27 \text{ Myr}$. The efficiencies of a continuous wind and sporadic individual SNe in driving large scale outflows are hard to compare because the models differ in their

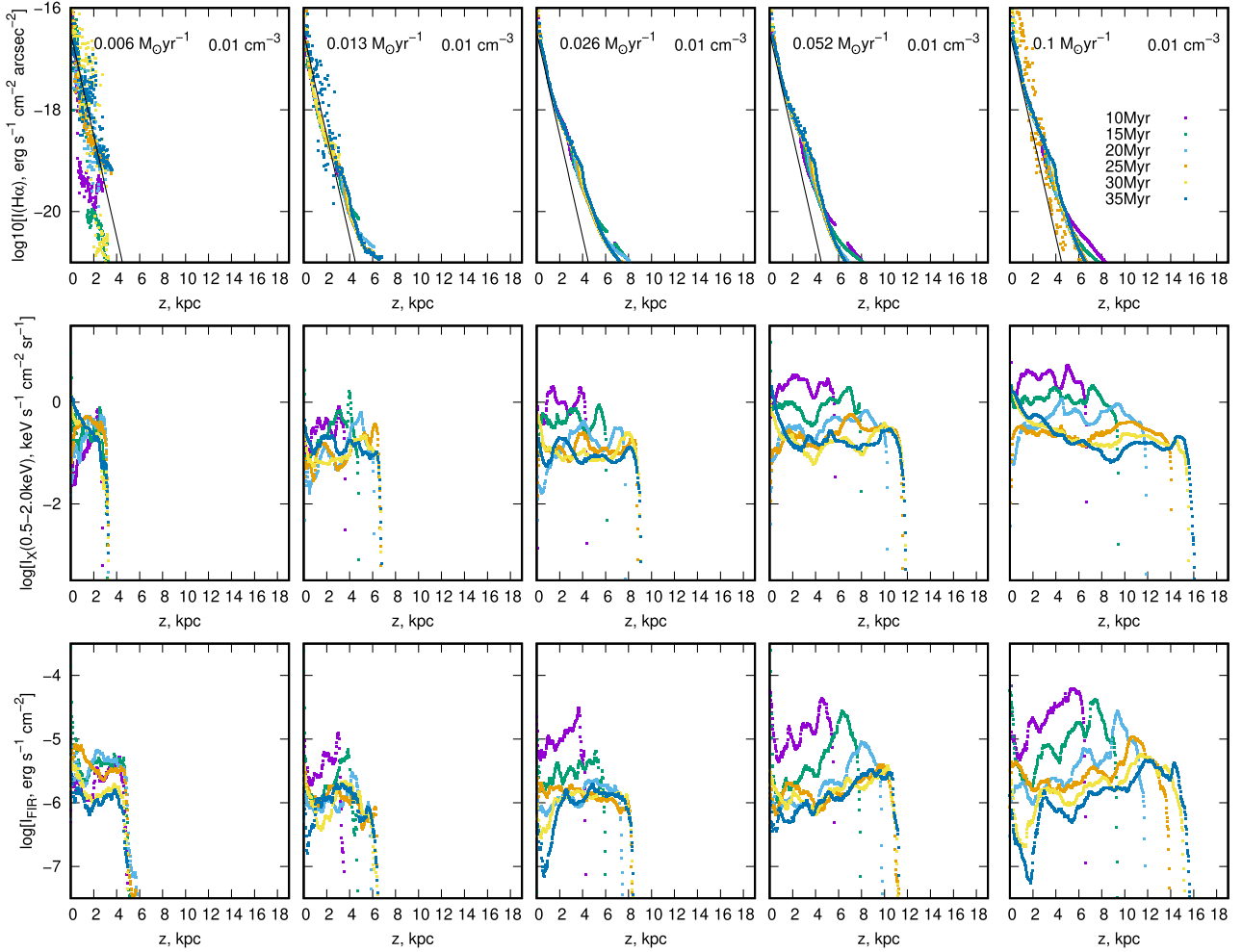


Figure 16. From the uppermost to the lowermost: Shown are the vertical profiles of $H\alpha$, X-ray (0.6–1 keV) intensities, and the IR flux in the range from $\lambda = 3 \mu\text{m}$ to 3 mm for different ages corresponding to the superbubbles in Fig. 5 (10, 15, 20, 25, 30, and 35 Myr, respectively, also shown in the upper right panel). The profiles are horizontally averaged at a given z within $\Delta r = 100 \text{ pc}$ centred at $r = 0$. In panels of $H\alpha$ intensity the thin black line depicts an exponential decrease $I \sim \exp(-z)$. Colours code the superbubble age equivalently to those in Fig. 5.

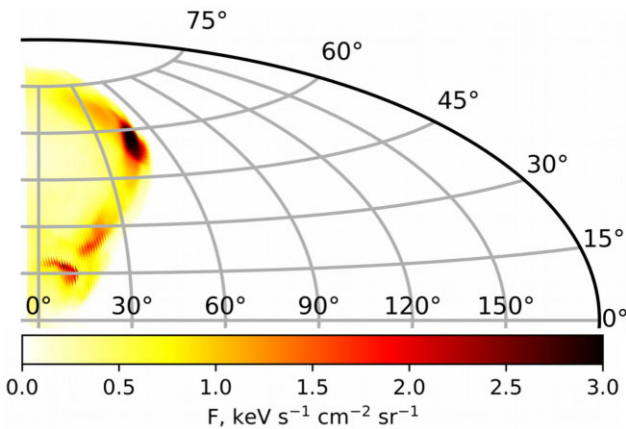


Figure 17. X-ray surface intensity ($\text{keV s}^{-1} \text{ cm}^{-2} \text{ sr}^{-1}$) in the range 0.7–1.2 keV in the galactic coordinates (an observer is located at 8 kpc from the centre of SNe cluster, which is in the galactic centre) for the model with $\text{SFR} = 0.1 M_{\odot} \text{ yr}^{-1}$. The age is 25 Myr. The halo profile is fiducial: $n_h = 10^{-2} \text{ cm}^{-3}$.

basic parameters: mid-plane disc densities, halo densities, and the corresponding scales.

It is worth noting that the expected brightness of the superbubble in our model is comparable in order of magnitude to the one obtained by Sarkar et al. (2015). For the leptonic mechanism of γ -emission connected with an inverse scattering of CMB photons on cosmic ray electrons with $E \sim 100 \text{ TeV}$, one can estimate the surface brightness of the bubble at γ -ray energy $E_{\gamma} \sim 1 \text{ GeV}$ as $F_{\gamma} \sim 6 \times 10^{-8} n_3 T_7 L_1 \text{ GeV cm}^{-2} \text{ s}^{-1} \text{ sr}^{-1}$, with the gas density $n_3 = 10^{-3} n$, and temperature $T_7 = 10^{-7} T$, and the line-of-sight thickness of the emitting hot gas $L_1 = L/1 \text{ kpc}$, following the assumption of Sarkar et al. (2015) that the cosmic ray electron energy density is proportional to the energy density of the hot gas.

4.2 Edge-on galaxies

Our results can be applied also to edge-on galaxies where growing bubbles and superbubbles are seen projected along a sightline, and in some cases, can be superimposed to form a smooth image along the galactic disc without being separated individually.

The superbubble X-ray brightness in the low energy band 0.5–2 keV band increases with the halo floor density ρ_h . This follows from

the dependence of emissivity on density: The intensity is roughly $I_x \sim 2R_b \epsilon_X(\rho, T)$, where $\epsilon_X \propto \rho_b^2 T^{-1/2} \exp(-1.16 E_{\text{keV}}/T_7)$ is the emissivity, $R_b \propto \rho_b^{-1/5}$ the bubble radius, $T \propto \rho_b^{-2/5}$. At later stages when the vertical size of the bubble is in excess of $\sim 2z_g$, it expands predominantly into the halo, and we assume that the mean gas density in the bubble is $\langle \rho_b \rangle \sim 10^{-2} \rho_h$ (Vasiliev et al. 2017). The exponential factor in the emissivity $e^{-2.33/T_7}$ determines a slow decay of the brightness in time.

Quite similarly $H\alpha$ emission increases with the halo density as the X-ray intensity does. It is connected with the fact that the recombination emissions come from the denser and colder shell with a dominant contribution from the regions belonging to the halo.

For a fixed gas halo density profile, the soft X-ray intensity of the bubbles shows rather a weak sensitivity to SFR in the range $0.05\text{--}0.1 M_\odot \text{ yr}^{-1}$, as seen in Fig. 10 and on the second row in Fig. 16: From left to right the z -averaged intensity shows only time variations from $\sim 1\text{--}2$ at $t = 10 \text{ Myr}$ to $\sim 0.1 \text{ keV cm}^{-2} \text{ s}^{-1} \text{ sr}^{-1}$ at $t = 35 \text{ Myr}$. This is connected with a weak dependence of the superbubble radius on SFR nearly as $R_b \propto \text{SFR}^{1/5}$. Another reason is that superbubbles with higher SFR expand progressively upwards after reaching a few z_h , and the gas density inside decreases faster than in those bubbles driven by lower SFR. However, when integrated over the superbubble, the total X-ray luminosity relates to the SFR as $L_X \propto \text{SFR}^\alpha$ with $\alpha \approx 0.25\text{--}1.3$ depending on the age (see Section 3.2.1).

Warm dust is also known to trace galactic outflows on scale heights from the inner and intermediate haloes (Dahlem et al. 2001; Tüllmann et al. 2006; McCormick, Veilleux & Rupke 2013) to larger heights reached by strong galactic winds. In the end of evolution, the integral IR luminosity of a single bubble with a given SFR (in $M_\odot \text{ yr}^{-1}$) is $L_{\text{IR}}/L_\odot \sim 2 \times 10^6 \text{ SFR}$ (see Fig. 9). This is strikingly lower (four order of magnitudes) than the $L_{\text{FIR}}\text{--SFR}$ relation for normal and starburst galaxies (see for recent discussion Kennicutt & Neal 2012; Kennicutt & De Los Reyes 2021). It is important to emphasize though that this relation belongs solely to the superbubble interior extending to the outer $z > 1 \text{ kpc}$ halo and is explained by a low gas density in there. On the contrary, FIR from starburst galaxies stems from the brightest regions of SF in the galaxy discs. Estimates of the extraplanar ($z \gtrsim 1 \text{ kpc}$) FIR emission in edge-on galaxies give similar numbers. For instance, the sum of the FIR fluxes from extraplanar regions around the X-shaped structure in the galaxy NGC 3079 with its $\text{SFR} \approx 2.6 M_\odot \text{ yr}^{-1}$ (Veilleux et al. 2021), results in $L_{\text{FIR}} \sim 2 \times 10^7 \text{ SFR}$ in solar units. A similar value $L_{\text{FIR}} \sim 4 \times 10^7 \text{ SFR}$ can be inferred from the data for the halo of the galaxy NGC 891 presented by Yoon et al. (2021; see their Table 3).

4.2.1 NGC 891

The galaxy NGC 891 is similar to the Milky Way (Bok & Bok 1981; van der Kruit 1984; Sofue, Nakai & Handa 1987; Bottema, van der Kruit & Valentijn 1991; Dettmar 1992; Dahlem et al. 1995). Its IR, $H\alpha$, CO, [CII] $158 \mu\text{m}$ emissions and the synchrotron radio-halo and other galaxy-scale structures are fed by $\text{SFR} \sim 5$ to $\sim 10 M_\odot \text{ yr}^{-1}$ (as inferred from Dahlem et al. 1995). Recently Yoon et al. (2021) described a FIR emission from a dusty halo extending up to 8 kpc above the disc. It may indicate that even though averaged over the disc surface SFR is only $\sim 0.03 M_\odot \text{ yr}^{-1} \text{ kpc}^{-2}$, under certain conditions, it can launch a large scale elevation of the interstellar gas. From the point of view of our simulations, such conditions can be fulfilled when the injection of energy into the interstellar medium (ISM) is provided by compact stellar clusters: About a hundred OB-

associations of $\sim 0.04 M_\odot \text{ yr}^{-1}$ with the total rate $\sim 4 M_\odot \text{ yr}^{-1}$ spread randomly over the disc can maintain such a halo. Indeed, as seen from Fig. 5, a cluster with $\text{SFR} = 0.04 M_\odot \text{ yr}^{-1}$ in 35 Myr reaches $z \sim 10 \text{ kpc}$ and $r \sim 4 \text{ kpc}$, covering in the disc $\sim 50 \text{ kpc}^2$. As seen in Fig. 4, the lifetime of such superbubbles can be longer than 35 Myr, resulting in a high covering fraction of the disc area by superbubbles. The total X-ray luminosity of such superbubbles can be of $10^{36}\text{--}10^{37} \text{ erg s}^{-1}$ each as can be judged from Fig. 9, being in agreement with observational estimates (Bregman & Pildis 1994; Wang et al. 1995).

Hodges-Kluck et al. (2018) report a disc-wide X-ray emission $E = 0.4\text{--}1.4 \text{ keV}$ with the intensity $\sim 10^{-15} \text{ erg cm}^{-2} \text{ s}^{-1} \text{ arcmin}^{-2}$ extending up to 5 kpc in the vertical direction, and up to 10 kpc in the central part; higher energy photons $E = 2\text{--}5 \text{ keV}$ extend over smaller distances. All our models except the one with $\text{SFR} = 0.026 M_\odot \text{ yr}^{-1}$ and $n_h = 0.001 \text{ cm}^{-3}$ (5th panel in Fig. 5) predict similar intensities within the heights they occupy. In particular, the model superbubble from a cluster with $\text{SFR} = 0.05 M_\odot \text{ yr}^{-1}$ extends its soft X-ray up to $z \sim 10 \text{ kpc}$ (see third panel in second row in Fig. 16). The latter may indicate on the presence of an active stellar cluster that might have initiated an outflow 25–30 Myr ago in the centre of NGC 891.

Intensities in $H\alpha$ predicted in all our models (except the one with $\text{SFR} = 0.026 M_\odot \text{ yr}^{-1}$ and $n_h = 0.001 \text{ cm}^{-3}$ on 5th panel in Fig. 5) within $|z| \sim 2\text{--}3 \text{ kpc}$ are consistent with those observed in edge-on galaxies in the sample reported by Miller & Veilleux (2003) including NGC 891.

The OVI 1036 Å line emission with $\lesssim 10^{-18} \text{ erg cm}^{-2} \text{ s}^{-1} \text{ arcmin}^{-2}$ at heights up to $z = 1.5 \text{ kpc}$ is also observed (Chung, Vargas & Hamden 2021). Absorptions in low-ionized ions typical for warm ionized gas (CII, MgII, SiII, SiIII, and others) has been observed by Qu, Bregman & Hodges-Kluck (2019).

5 CONCLUSIONS

Our results are summarized as follows:

- (i) Stellar clusters with $\text{SFR} = 0.006\text{--}0.1 M_\odot \text{ yr}^{-1}$ and surface energy injection rate of $\dot{\epsilon} \sim 0.01\text{--}0.15 \text{ erg cm}^{-2} \text{ s}^{-1}$ produce superbubbles extending from 3 to 16 kpc. The superbubble traced in the Milky Way by the North Polar Spur can be launched and maintained by a cluster with a relatively low $\text{SFR} \sim 0.1 M_\odot \text{ yr}^{-1}$ close to the observed one. The value of the $\text{SFR} \sim 0.006 M_\odot \text{ yr}^{-1}$ and the corresponding energy input rate $\dot{\epsilon} \sim 0.01 \text{ erg cm}^{-2} \text{ s}^{-1}$ is close to the threshold in ambient gas with parameters typical for the Milky Way central region.
- (ii) Such superbubbles can stay filled with a hot ($T \gtrsim 10^6\text{--}10^7 \text{ K}$) low-density ($n \lesssim 10^{-3} \text{ cm}^{-3}$) and enriched ($[Z/H] \gtrsim 0$) gas for a long time of the order of $t \gtrsim 30 \text{ Myr}$, and be sufficiently bright in the soft X-ray emission in energy range $E = 0.5\text{--}2.0 \text{ keV}$ with $L_X \sim (0.1\text{--}1) \times 10^{36} \text{ SFR}^{4/3} \text{ erg s}^{-1}$ while $\text{SFR} \lesssim 0.06 M_\odot \text{ yr}^{-1}$, and $L_X \sim (2\text{--}6) \times 10^{37} \text{ SFR}^{1/4} \text{ erg s}^{-1}$ at higher SFR.
- (iii) A fraction of dust can survive in the bubble interior on this time scale, and can be seen in infrared emission. However, a deficit of dust particles of small sizes $a \lesssim 100 \text{ \AA}$ results in a considerable, factor of ten, depression of the integrated dust IR emission, even though the dust mass remains practically unchanged. The deficit of small size particles is also revealed in the ratio $F_\lambda(25 \mu\text{m})/F_\lambda(250 \mu\text{m})$. The ‘normal’ dust shows $\log [F_{25}/F_{250}] \approx 0.8$, whereas the ‘burnt’ one has $\log [F_{25}/F_{250}] \approx 0.5$.
- (iv) Stellar clusters with SFR in this range spread through over galactic discs can maintain gaseous haloes that radiates in X-ray,

$H\alpha$, and IR dust continuum with the intensities similar to those observed in edge-on galaxies (such as NGC 891). The luminosity of individual superbubbles is connected with the underlying SFR $L_{\text{IR}}/L_{\odot} \sim 2 \times 10^6$ SFR, roughly consistent with the halo IR-emission observed in a few edge-on galaxies.

ACKNOWLEDGEMENTS

We thank the referee, R. Wünsch, for his friendly criticism and valuable comments. The work by SD and YS is done under partial support from the pro ‘New Scientific Groups LPI’ 41-2020. The numerical simulations have been performed in the High Performance Cluster at the Raman Research Institute, Bangalore.

DATA AVAILABILITY

The data underlying this article are available in the article.

REFERENCES

- Alton P. B. et al., 2000, *A&AS*, 145, 83
 Bakes E. L. O., Tielens A. G. G. M., 1994, *ApJ*, 427, 822
 Barnes A. T. et al., 2017, *MNRAS*, 469, 2263
 Berkhuijsen E. M. et al., 1971, *A&A*, 14, 359
 Bianchi S., Schneider R., 2007, *MNRAS*, 378, 973
 Bocchio M., Bianchi S., Hunt L. K., Schneider R., 2016, *A&A*, 586, A8
 Bok J. B., Bok P. F., 1981, *The Milky Way*. Harvard Univ. Press, Cambridge, MA
 Bordoloi R. et al., 2014, *ApJ*, 796, 136
 Bottema R., van der Kruit P. C., Valentijn E. A., 1991, *A&A*, 247, 357
 Bregman J. N., Pildis R. A., 1994, *ApJ*, 420, 570
 Burchett J. N. et al., 2015, *ApJ*, 815, 91
 Burke J., Silk J., 1974, *ApJ*, 190, 1
 Chung H., Vargas C. J., Hamden E., 2021, *ApJ*, 916, 7
 Dahlem M., Lisenfeld U., Golla G., 1995, *ApJ*, 444, 119
 Dahlem M., Lazendic J. S., Haynes R. F., Ehle M., Lisenfeld U., 2001, *A&A*, 374, 42
 Dahlem M., Lisenfeld U., Rossa J., 2006, *A&A*, 457, 121
 de Avillez M. A., 2000, *MNRAS*, 315, 479
 Dettmar R.-J., 1992, *Fundam. Cosm. Phys.*, 15, 143
 Dobler G. et al., 2010, *ApJ*, 717, 825
 Draine B. T., 1981, *ApJ*, 245, 880
 Draine B. T., 2011, *Physics of the Interstellar, Intergalactic Medium*. Princeton Univ. Press, Princeton, NJ
 Draine B. T., Salpeter E. E., 1979, *ApJ*, 231, 77
 Dwek E., 1981, *ApJ*, 247, 614
 Dwek E., 1986, *ApJ*, 302, 363
 Dwek E., Arendt R., 1992, *ARA&A*, 30, 11
 Federrath C. et al., 2016, *ApJ*, 832, 143
 Fielding E., Quataert E., Martizzi D., 2018, *MNRAS*, 481, 3325
 Franeck A. et al., 2022, *ApJ*, 927, 14
 Gall C. et al., 2014, *Nature*, 511, 326
 Girichidis P. et al., 2016, *MNRAS*, 456, 3432
 Hanbury Brown R., Davies R. D., Hazard C., 1960, *Observatory*, 80, 191
 Haslam C. G. T., Salter C. J., Stoffel H., Wilson W. E., 1983, *A&AS*, 47, 1
 Heckman T. M., 2000, *Phil. Trans. R. Soc. A*, 358, 2077
 Hill A. S. et al., 2012, *ApJ*, 750, 104
 Hodges-Kluck E. J., Bregman J. N., Li J.-t., 2018, *ApJ*, 866, 126
 Howk J. C., Savage B. D., 1999, *AJ*, 117, 2077
 Hughes T. M. et al., 2014, *A&A*, 565, A4
 Iben I., 2012, *Stellar Evolution Physics, Volume 1: Physical Processes in Stellar Interiors*. Cambridge Univ. Press, Cambridge
 Immer K., Schuller F., Ommont A., Menten K. M., 2012, *A&A*, 537, A121
 Jones A. P., Tielens A. G. G. M., Hollenbach D. J., McKee C. F., 1994, *ApJ*, 433, 797
 Kalberla P. M. W., Kerp J., 2009, *ARA&A*, 47, 27
 Keeney B. A. et al., 2017, *ApJS*, 230, 6
 Kennicutt R. C., Jr, De Los Reyes M. A. C., 2021, *ApJ*, 908, 61
 Kennicutt R. C., Jr, Neal J. E. II, 2012, *ARA&A*, 50, 531
 Klingenberg Ch., Schmidt W., Waagan K., 2007, *J. Comp. Phys.*, 227, 12
 Koepferl C. M., Robitaille T. P., Morales E. F. E., Johnston K. G., 2015, *ApJ*, 799, 53
 Kruijssen J. M. D., 2017, *IAU Symp. 322, The Multi-Messenger Astrophysics of the Galactic Centre*. Cambridge Univ. Press, Cambridge, UK, p. 64
 Krumholz M. R., Kruijssen J. M. D., 2015, *MNRAS*, 453, 739
 Krumholz M. R., Kruijssen J. M. D., Crocker R. M., 2016, *MNRAS*, 466, 1213
 Krumholz M. R., McKee C. F., Bland-Hawthorn J., 2019, *ARA&A*, 57, 227
 Laor A., Draine B. T., 1993, *ApJ*, 402, 441
 Lau R. et al., 2015, *Science*, 348, 413
 Lehnert M. D., Heckman T. M., 1996a, *ApJ*, 462, 651
 Li J.-T. et al., 2017, *ApJS*, 232, 20
 Li M., Bryan G. L., Ostriker J. P., 2017, *ApJ*, 841, 101
 McCormick A., Veilleux S., Rupke D. S. N., 2013, *ApJ*, 774, 126
 Mathis J. S., Rumpl W., Nordsieck K. H., 1977, *ApJ*, 217, 425
 Matsuura M. et al., 2011, *Science*, 333, 1258
 Miller M. J., Bregman J. N., 2015, *ApJ*, 800, 14
 Miller S. T., Veilleux S., 2003, *ApJS*, 148, 383
 Nath B. B., Shchekinov Y. A., 2013, *ApJ*, 777, L12
 Oosterloo T., Fraternali F., Sancisi R., 2007, *AJ*, 134, 1019
 Predehl P. et al., 2020, *Nature*, 588, 227
 Prochaska J. X., Weiner B. J., Chen H.-W., Mulchaey J. S., 2006, *ApJ*, 643, 680
 Prochaska J. X. et al., 2017, *ApJ*, 837, 169
 Qu Z., Bregman J. N., Hodges-Kluck E. J., 2019, *ApJ*, 876, 101
 Rossa J., Dettmar R.-J., 2000, *A&A*, 359, 433
 Rossa J., Dettmar R.-J., Walterbos R. A. M., Norman C. A., 2004, *AJ*, 128, 674
 Roy R., Nath B. B., Sharma P., Shchekinov Y. A., 2013, *MNRAS*, 434, 3572
 Sarkar K. C., Nath B. B., Sharma P., 2015, *MNRAS*, 453, 3827
 Seon K.-I., Witt A. N., Shinn J.-H., Kim I.-J., 2014, *ApJ*, 785, L18
 Sharma P., Roy A., Nath B. B., Shchekinov Y. A., 2014, *MNRAS*, 443, 3463
 Shchekinov Y., 2018, *Galaxies*, 6, 62
 Shinn J.-H., 2018, *ApJS*, 239, 21
 Simcoe R. A., Sargent W. L. W., Rauch M., Becker G., 2006, *ApJ*, 637, 648
 Sofue Y., 1994, *ApJ*, 431, L91
 Sofue Y., Nakai N., Handa T., 1987, *PASJ*, 39, 47
 Su M., Slatyer T. R., Finkbeiner T. P., 2010, *ApJ*, 724, 1044
 Temple R. F., Raychaudhury S., Stevens I. R., 2005, *MNRAS*, 362, 581
 Tielens A. G. G. M., McKee C. F., Seab C. G., Hollenbach D. J., 1994, *ApJ*, 431, 321
 Todini P., Ferrara A., 2001, *MNRAS*, 325, 726
 Toro E., 1999, *Riemann solvers, numerical methods for fluid dynamics*, 2nd edn. Springer-Verlag, Berlin
 Tüllmann R., Breitschwerdt D., Rossa J., Pietsch W., Dettmar R.-J., 2006, *A&A*, 457, 779
 Tumlinson J., Thom C., Werk J. K., 2011, *Sci.*, 334, 948
 van der Kruit P. C., 1984, *A&A*, 140, 470
 Vasiliev E. O., 2011, *MNRAS*, 414, 3145
 Vasiliev E. O., 2013, *MNRAS*, 431, 638
 Vasiliev E. O., Nath B. B., Shchekinov Yu. A., 2015, *MNRAS*, 446, 1703
 Vasiliev E. O., Shchekinov Yu. A., Nath B. B., 2017, *MNRAS*, 468, 2757
 Vasiliev E. O., Shchekinov Yu. A., Nath B. B., 2019, *MNRAS*, 486, 3685
 Veilleux S. et al., 2021, *MNRAS*, 508, 4902
 Walch S. et al., 2015, *MNRAS*, 454, 238
 Wang Q. D. et al., 1995, *ApJ*, 439, 176
 Yadav N., Mukherjee D., Sharma P., Nath B. B., 2017, *MNRAS*, 465, 1720
 Yoon J. H. et al., 2021, *MNRAS*, 502, 969
 Yusef-Zadeh F. et al., 2009, *ApJ*, 702, 178

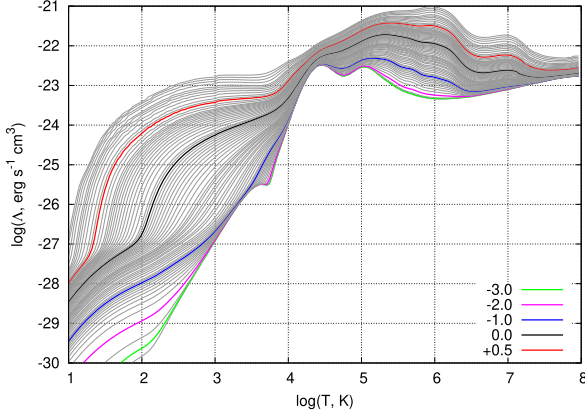


Figure A1. Isochoric cooling rates in the metallicity range $[Z/H]=-4..1$ with the increment $[\Delta Z/H]$, calculated using the method described in Vasiliev (2013).

APPENDIX A: COOLING FUNCTION

In our simulations we have used a non-equilibrium cooling function $\Lambda(T, Z)$ that includes time-dependent evolution of the ionization state of the dominant coolants: He, C, N, O, Ne, Mg, Si, Fe, implemented self-consistently into cooling processes described by Vasiliev (2013), Z is the abundance of heavy elements. In (Vasiliev 2013) calculations of the gas ionization and thermal state begin from the initial conditions at $T = 10^8$ K when all dominant elements are fully ionized and then are supposed to recombine free without additional ionization and heating sources. We make use only the isochoric version of the cooling function because hydrodynamical processes relax to pressure equilibrium on relevant time-scales of a Myr. In our simulations the $\Lambda(T, Z)$ function is tabulated properly and when necessary, splined between different T and Z corresponding to their values in a given cell and at a given time. Fig. A1 shows a graphical representation of $\Lambda(T, Z)$, the increment $[\Delta Z/H]$ is

calculated from the requirements that

$$\Delta\Lambda(T, Z) = \frac{1}{\Lambda(T, z)} \frac{\partial\Lambda(T, Z)}{\partial[Z/H]} [\Delta Z/H] \leq -0.04, \quad (\text{A1})$$

resulting in an approximate difference between subsequent values of $\Lambda(T, Z)$ by not more than 10–12 per cent.

APPENDIX B: EVOLUTION OF DUST SIZE DISTRIBUTION

At $T > 10^6$ K thermal sputtering rate of a dust particle is $\dot{a} \simeq -3 \times 10^{-18} n \text{ cm s}^{-1}$, \dot{a} does not depend explicitly on dust radius a . Correspondingly, the continuity equation for dust size distribution is (equation 72 in Laor & Draine 1993)

$$\frac{\partial n_a}{\partial t} + \dot{a} \frac{\partial n_a}{\partial a} = 0, \quad (\text{B1})$$

it has the solution $n_a(t) = f(a + a_0 t / \tau_0)$, where $a_0 / \tau_0 \equiv 3 \times 10^{-18} n$, $f(a)$ is the dust size distribution at the initial state. For the ‘standard’ MRN distribution $n_a \propto a^{-3.5}$ within $a_1 \leq a \leq a_2$ (Mathis et al. 1977) the distribution remains similar $n_a(t) \propto (a + a_0 t / \tau_0)^{-3.5}$ with a decreasing magnitude and with the minimum size $a_a(t) = a_1 + a_0 t / \tau_0$.

This paper has been typeset from a $\text{\TeX}/\text{\LaTeX}$ file prepared by the author.